

Boosting the Mechanical and Electrochemical Performance of MnO_2 Dry Electrode with Bentonite for Ampere-Hour Aqueous Zn-ion Batteries

Haitao Zhou,*^[a] Huanggang Wang,^[a] Jian-Chun Wu,*^[a] Hongquan Gao,^[a] Haiyun Zhou,^[b] Yafei Shi,^[a] and Jie Gu^[a]

Aqueous zinc-ion batteries, distinguished by their robust safety, abundance, and cost-effectiveness, represent an ideal solution for wearable devices, backup power sources, and microgrid energy storage applications. Among various cathode materials, MnO_2 stands out as one of the most promising candidates due to its high potential relative to Zn, high theoretical specific capacity, low cost, and non-toxicity. However, the electrochemical performance of MnO_2 cathode is hindered by Mn death and pH fluctuations. Additionally, the internal inhomogeneity resulting from solvent evaporation during the slurry coating process further compromises their stability. In this study, we introduce a modification using sodium-based bentonite and successfully fabricate high-loading industrial-

grade electrolytic MnO_2 cathode through a pilot-scale solvent-free dry process. The sodium-based bentonite enhances the structural stability of the electrode by forming Na–F bonds with polytetrafluoroethylene and optimizes Zn^{2+} transport through its ion-exchange properties to regulate pH. Impressively, high-loading Ben-SFC//Zn battery, with a loading exceeding 10 mg cm^{-2} , maintains a coulombic efficiency above 98% and capacity of 80% after approximately 400 cycles. Similarly, a 3Ah aqueous pouch cell demonstrates stable cycling over 400 cycles. This research not only addresses the challenges in manufacturing process of practical high-loading MnO_2 dry electrodes but also elevates the electrochemical performance of batteries.

1. Introduction

The field of energy storage batteries for renewable energy microgrids and backup power supplies has traditionally been dominated by lead-acid batteries.^[1] However, due to their environmental unfriendliness, pollution from heavy metals and strong acids, limited cycle life, and performance decline during prolonged storage, they are gradually being replaced by lithium-ion batteries. Although the substantial cost reduction of lithium-ion batteries, particularly LiFePO_4 , which has fueled their substitution for lead-acid batteries as a prevalent trend in this field, challenges such as inadequate safety performance, storage capabilities, the scarcity and uneven distribution of lithium resources^[2] have hindered their widespread market acceptance. Furthermore, in crucial sectors with exceptionally high safety standards such as maritime navigation, medical equipment and data storage, water-based lead-acid batteries continue to occupy an irreplaceable significant position. Therefore, the pursuit of low-cost, highly secure, long-lasting and

inherently eco-friendly new aqueous-based batteries^[3] has emerged as a focal point of intense research within the industry.

In recent years, aqueous Zn-ion batteries (AZIBs) have attracted considerable attention owing to their unique advantages.^[4] By employing non-flammable aqueous solutions as electrolytes and utilizing Zn metal as anode, these batteries offer a combination of low cost, abundant reserves, high theoretical specific capacity (820 mAh g^{-1} in mass specific capacity and 5855 mAh cm^{-3} in volume specific capacity), and low equilibrium potential (-0.762 V vs. standard hydrogen electrode). These attributes render AZIBs highly promising for applications in future small electric vehicles and wearable electronic devices.^[5] Consequently, finding an efficient cathode material for Zn^{2+} storage in neutral aqueous solutions has become a focal point for researchers. Currently, MnO_2 ,^[6-7] V_2O_5 ,^[8-9] and Prussian blue analogues^[10-11] have been reported for Zn^{2+} storage, with MnO_2 emerging as the most potential cathode material for AZIBs owing to its high theoretical specific capacity (308 mAh g^{-1}), acceptable voltage platform (1.35 V vs. Zn^{2+}/Zn), low cost, and non-toxicity. Diversity in the connectivity of $[\text{MnO}_6]$ unit results in various tunnel/layered crystal structures, including $\alpha\text{-MnO}_2$, $\beta\text{-MnO}_2$, $\gamma\text{-MnO}_2$, and $\delta\text{-MnO}_2$. However, different electrochemical behaviors of polymorphic MnO_2 during Zn^{2+} storage complicate its energy storage mechanisms, which primarily encompass insertion-deintercalation mechanisms,^[12-16] conversion reactions,^[17-19] and dissolution-deposition mechanisms.^[20-21] Regardless of the initial crystal structure, MnO_2 hosts undergo irreversible structural deformations, even collapsing or powdering, during charge-discharge

[a] Assoc. Prof. H. Zhou, H. Wang, Assoc. Prof. J.-C. Wu, Prof. H. Gao, Y. Shi, J. Gu

School of Materials Science and Engineering, Jiangsu University, 212013, Zhenjiang, Jiangsu Province, P. R. China

E-mail: haitao1985@ujs.edu.cn
jcwu@ujs.edu.cn

[b] H. Zhou
Jiangsu Tongling Electric Co., Ltd., 212200, Jiangsu Province, Zhenjiang, Jiangsu Province, P. R. China

 Supporting information for this article is available on the WWW under <https://doi.org/10.1002/batt.202400757>

cycles. These structural changes are accompanied by significant pH fluctuations and side reactions, resulting in rapid capacity fade and a substantial decline in coulombic efficiency. These issues are mainly attributed to insertion/deintercalation of $[Zn(H_2O)_6]^{2+}$ and H_3O^+ or dissolution of manganese. Fortunately, advancements and applications of nanotechnology^[22] provide fresh perspectives for enhancing the performance of Zn//MnO₂ secondary batteries. Nanoscale silica-based materials, especially naturally occurring clay minerals such as kaolin and bentonite,^[23] exhibit layered structures characterized by high specific surface energy due to the periodic stacking of silica-oxygen and alumina (or magnesia) layers. These materials are frequently employed to modify^[24–26] matrix materials, thereby optimizing their strength, toughness, modulus, swelling capacity, ion exchange properties and other characteristics. For instance, Zhou *et al.*^[27] designed a kaolin-coated Zn anode (KL-Zn) with Zn²⁺-selective channels and uniform pore distribution. Abundant O-H and Si-O bond adsorption sites within this anode/electrolyte interface layer capture and direct Zn²⁺ migration and deposition in a limited direction on the anode side. As a result, KL-Zn exhibits high self/electrochemical corrosion resistance and dendrite suppression capability in both symmetric cells and practical full-cell configurations. More importantly, the KL-Zn//MnO₂ battery maintains excellent cycle stability and rate performance after long-term cycling, with well-preserved Zn anode morphology. Additionally, to enhance the energy density and efficiency of Zn//MnO₂ secondary batteries that utilize traditional slightly acidic or near-neutral liquid electrolytes, the team proposed an innovative ion concentration/dilution strategy.^[28] By mixing the conventional liquid electrolyte comprising ZnSO₄ and MnSO₄ with negatively charged bentonite, they obtained a bentonite colloid (Ben-colloid) electrolyte. Capitalizing on ion exchange properties of bentonite, Zn/Mn ion exchange on the cathode side regulates Mn ion concentration, stimulating two-electron Mn⁴⁺/Mn²⁺ redox reaction for additional deposition/dissolution capacity. Batteries employing Ben-colloid electrolytes demonstrate significant improvements in electrochemical performance compared to conventional liquid electrolyte systems, exhibiting a significant enhancement in specific capacity, along with superior rate capability, exceptional cycling stability, and remarkable thermal resilience. Furthermore, while the Ben-colloid electrolyte demonstrates remarkable advantages in stabilizing pH values, suppressing hydrogen evolution, and enhancing Zn deposition/stripping efficiency (> 98 %), its application in cathode preparation remains challenging. Although the mechanistic understanding of clay minerals in Zn anodes and electrolytes has advanced significantly, their direct utilization in MnO₂ cathode fabrication is still limited. Conventional wet slurry coating processing of MnO₂ electrodes inevitably leads to structural defects, including binder migration and conductive additive segregation during solvent evaporation, which typically reduces electrode mechanical strength and capacity retention. The inherent incompatibility between bentonite and MnO₂ fine powders exacerbates these issues, often resulting in non-Newtonian slurry behavior that hinders uniform coating and compromises manufacturing reproducibility. While dry elec-

trode technology^[29–32] presents a promising alternative, its effectiveness is constrained by the insufficient entanglement of fine active material particles (nanosized MnO₂ and conductive carbons) with fibrous PTFE, yielding electrodes with inadequate mechanical properties and poor flexibility. These technical limitations underscore the urgent need for innovative approaches to optimize MnO₂ electrode fabrication processes.

In this study, we designed cathode by using commercial electrolytic MnO₂ powder and sodium-based bentonite as the active material and modifying additive, respectively. The electrode was fabricated based on a solvent-free dry process^[33–37] previously reported by our research group, denoted as bentonite-solvent-free-cathode (Ben-SFC). Bentonite significantly enhanced the tensile strength and internal network of the cathode film. Density functional theory (DFT) calculations reveal that bentonite exhibits a crucial bridging effect between PTFE and KS-6 conductive graphite, significantly optimizing interfacial binding. Additionally, High-loaded Ben-SFC//Zn battery (exceeding 10 mg cm⁻²) maintained stable cycling for approximately 400 cycles and exhibited excellent rate performance. The inherent ion-exchange characteristics of bentonite optimized the Zn²⁺ transport efficiency within the electrode, regulated the pH value of the cathode, and minimized side reactions. This research provides a practical strategy for constructing MnO₂ electrode, effectively addressing manufacturing challenges and enhancing the electrochemical performance of, laying a foundation for future applications.

Experimental Work

Preparation of Ben-MnO₂-SFC: The preparation process is illustrated in Figure S1. Initially, granular powders including MnO₂, nano-sized sodium-based bentonite (200–500 nm), KS-6 conductive graphite, and PTFE are weighed according to the mass fraction ratio of 79:X:Y:4 (where X represents the Ben content, varying from 0 to 8, X=0 indicates no Ben added; Y represents the content of the conductive agent, satisfying X+Y=17). These materials are then pre-mixed using a VC mixer at 0–5 °C to ensure uniform dispersion. Subsequently, high-speed dry air is employed as the shearing force to accelerate the raw material mixture through a Laval nozzle for PTFE fibrillation. In addition to the air fibrillation process, we have incorporated a kneading step utilizing a kneading machine, with the aim of further promoting the fibrillation of PTFE. This results in the formation of a tightly entangled fibrous network that effectively encapsulates the other raw material particles, ultimately achieving uniform granulation. Next, the granular material is hot-rolled at 130 °C to form a self-supporting MnO₂/graphite self-standing film. Finally, the self-supporting film is laminated with a graphite-protected stainless steel current collector using another horizontal hot-rolling device at 90 °C to obtain the Ben-MnO₂-SFC. The graphite-protected stainless steel current collector is prepared based on our previous work,^[38] where water-resistant and acid-corrosion-resistant graphite adhesive is uniformly coated onto the surface of a stainless steel foil.

The detailed preparation work of Zn-In alloying powder solvent-free electrodes (Zn@In SFA), characterization works of physico-chemical properties and electrochemical properties and computational works are illustrated in the Supporting Information.

2. Results and Discussion

2.1. Materials Characterization

Figure 1a presents the macroscopic morphological changes of the cathode materials after air-flow fibrillation and subsequent kneading and granulation in a mixer under different Ben content conditions. Specifically, as Ben content increases, the morphology of the material particles gradually evolves from a fine and uniformly dispersed state (corresponding to 0% and 1% Ben content) to a large-sized, tightly aggregated form (especially when Ben content reaches 7%). Notably, at 4% Ben content, small particles are observed to spontaneously aggregate into relatively stable but not fully 'solidified' clumps. This transitional stage provides crucial clues for the film-forming property of cathode materials through rolling process. At low Ben content, the interaction between particles is weak, making it difficult to form easy-to-roll and formable particles. Conversely, high Ben content, owing to the strong adhesive

properties of bentonite itself, promotes excessive particle aggregation, resulting in 'solidified' clumps that impair the overall processability of material.

After placing the mixed granular material into the hopper of a high-precision hot roller press, we are able to produce MnO_2 /graphite self-standing film with a length of 100 m, a width of 15 cm, and a thickness of 90 μm at a speed of 2 m min^{-1} , as shown in (Figure S1 and Movie S1). Furthermore, as illustrated in Figure 1b, the roller-pressed films with different Ben content were cut into same size (20*100 mm) for tensile performance testing, which provided detailed data on Young's modulus (E) and tensile strength (σ_b). We found that the E and σ_b values of 0% Ben film was $28.5 \pm 3.0 \text{ MPa}$ and $0.26 \pm 0.08 \text{ MPa}$, respectively. With Ben content increased, both indicators showed an initial upward trend followed by a subsequent decline, peaking at a Ben content of 4%, where E soared to $94.2 \pm 11.8 \text{ MPa}$ and σ_b also improved to $0.57 \pm 0.12 \text{ MPa}$.

Compared with 0% Ben film, the mechanical properties have been improved by three times.

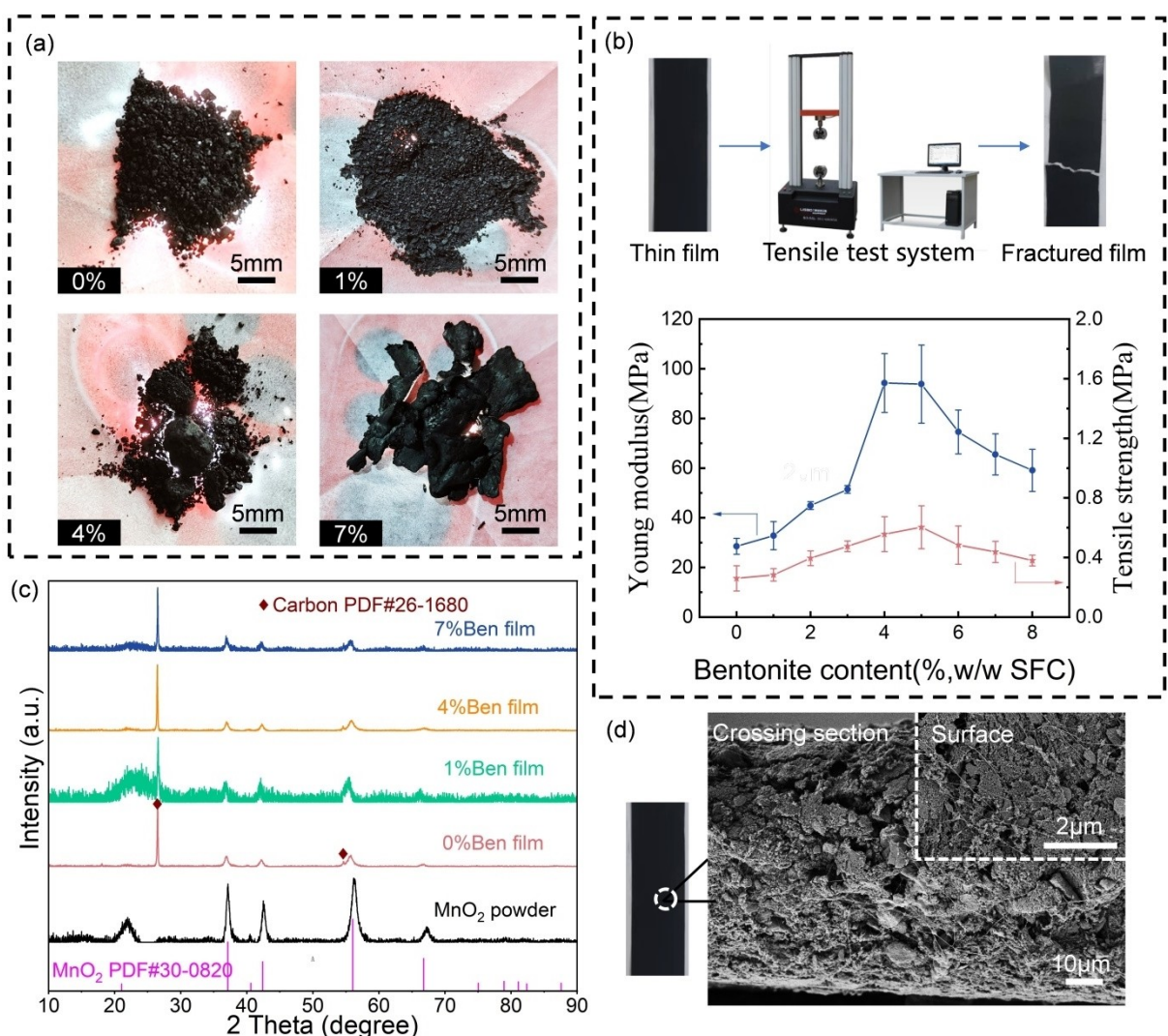


Figure 1. Characteristics of particles, Tensile properties and Morphological features of self-standing film prepared via a solvent-free process. a) Macroscopic morphology of particles at different Ben contents. b) Tensile properties of MnO_2 /graphite self-standing film with different Ben content. c) XRD pattern of MnO_2 powder and MnO_2 /graphite self-standing film with different Ben content. d) SEM images of crossing section and surface of 4% Ben film.

Adding an appropriate amount of Ben can optimize initial aggregation structure of the cathode material mixture, significantly enhancing the cohesion and mechanical strength of the film. However, an excessively high content of Ben can lead to an overly dense particle structure, making it difficult for the particles to undergo deformation during the rolling process, thereby affecting the mechanical properties of the thin film. As shown in Figure 1c, the diffraction angles corresponding to the characteristic peaks of MnO_2 ^[39] consistently shift towards smaller angles in MnO_2 /graphite self-standing films with different Ben content. According to Bragg's equation, this indicates an increase in the lattice spacing of the cathode material, which facilitates the rapid diffusion of Zn^{2+} and mitigates the structural damage to the cathode material during the insertion and extraction of Zn^{2+} . Meanwhile, when the incorporation level of bentonite varies from 0 to 7%, no significant changes are observed in the diffraction angles of the film, indicating that the crystal structure of MnO_2 remains relatively stable within this range of bentonite incorporation. SEM images (Figure 1d and Figure S3) reveal the cross-sectional and surface microstructural characteristics of each different Ben content film.

Utilizing a solvent-free process, the fibrillated PTFE binder adeptly intertwines MnO_2 powder, KS6 conductive graphite, and Ben particles into a complex network structure. Notably, 4% Ben film formulation exhibits a more abundant three-dimensional interwoven morphology. This configuration structure not only expands electrochemical active area but also effectively facilitates Zn ion diffusion.

To enhance our comprehension of how bentonite influences the mechanical attributes of MnO_2 /graphite self-standing film, Figure 2a illustrates the ball-and-stick model of sodium-based bentonite particles employed in this study. Ben particles are typical of a dioctahedral complex tri-layered silicate structure, consisting of two layers of silicon tetrahedra sandwiching a gibbsite layer as the fundamental structural unit, arranged periodically along c-axis. The partial substitution of Al^{3+} ions within these layers by ions such as Mg^{2+} induces a slight negative charge within the phyllosilicate layers, resulting in repulsive forces that encourage the interlayer incorporation of hydrated sodium ions. Moreover, the layers are held together by relatively weak intermolecular forces, enabling the easy permeation of water molecules, which consequently leads to an

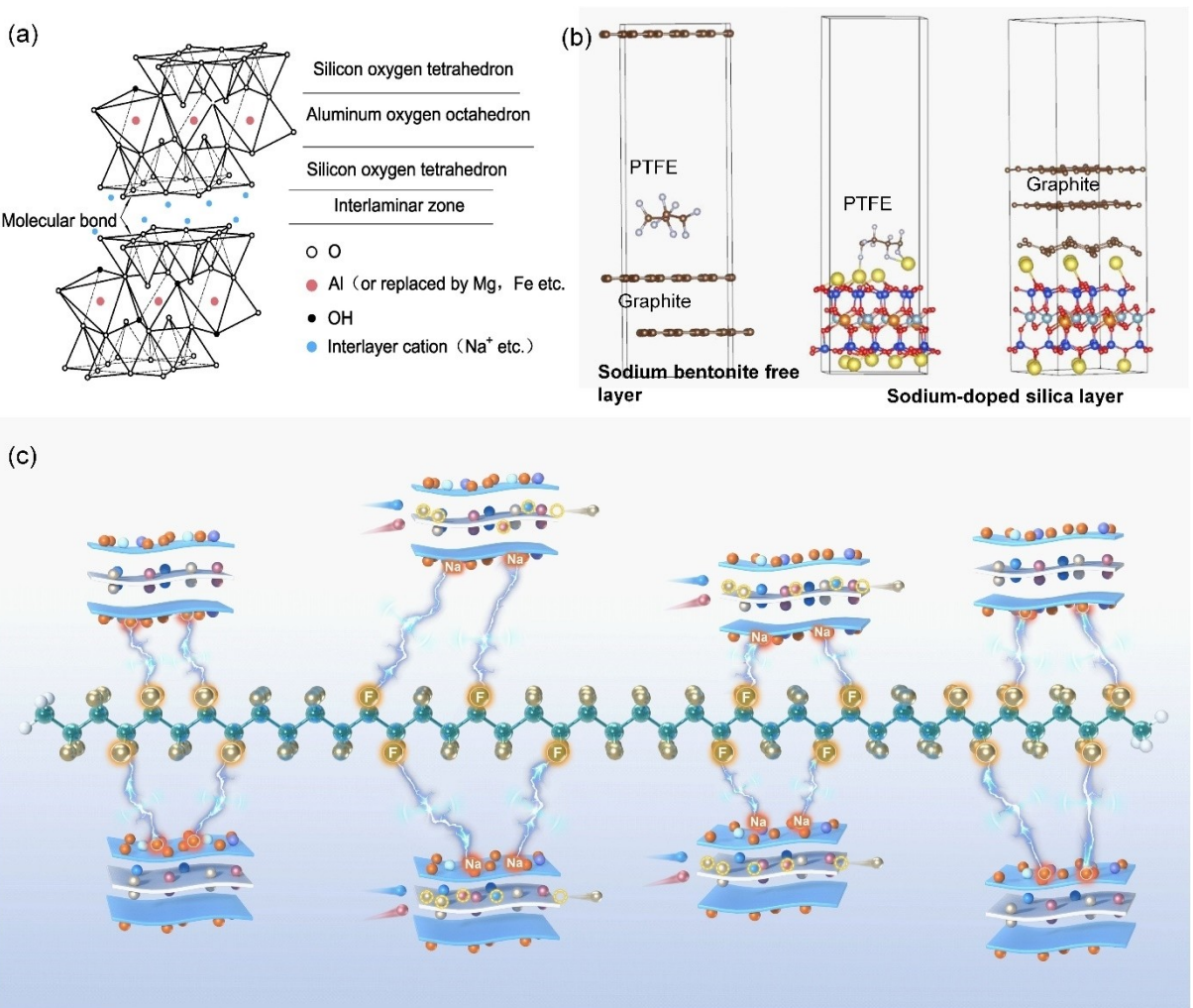


Figure 2. Basic structure and mechanism of Nano-sized Sodium-based bentonite. a) Ball-and-stick model of Sodium-based bentonite. b-c) Simulated calculation of the bridge effect of $\text{Na}-\text{F}$ bonds on constructing a 3D network inside MnO_2 /graphite self-standing film.

expansion of unit cell dimension along c-axis. This unique structure grants Ben particles structure an extensive specific surface area and a well-developed pore system, thereby significantly facilitating H^+ and Zn^{2+} ions transport on the cathode side.

The optimized structures of adsorption interaction between KS-6 graphite, bentonite, and PTFE, calculated using Density Functional Theory (DFT). As shown in Figure 2b, it can be observed that the bonding between PTFE and graphite is relatively weak, accompanied by minimal structural alterations in both materials, further indicating a weak adsorption effect. Conversely, for the interaction between PTFE and Ben, a distinct bridged association (Figure 2c) formed by Na atoms becomes evident. Similarly, there is a notable structural deformation between graphite and Na atoms in Ben. These observations collectively suggest that the formation of robust interactions between PTFE and Ben, as well as between graphite and bentonite. From an energetic perspective, the adsorption energy between graphite and PTFE stands at merely -0.21 eV , in stark contrast to the substantial adsorption energy of -10.70 eV between bentonite and PTFE. Furthermore, the adsorption energy between graphite and bentonite reaches an impressive -22.95 eV . These figures unequivocally demonstrate that bentonite serves as an adhesive, capable of firmly binding graphite and PTFE together.

To verify the accuracy of theoretical calculations, we conducted X-ray Photoelectron Spectroscopy (XPS) analysis on the mixtures of sodium-based bentonite and polytetrafluoroethylene (PTFE) at three stages: homogeneous mixing, fibrillation, and kneading. As shown in Figure 3, the peak of metal carbonate observed at a binding energy of 288.76 eV in the C 1s spectrum is attributed to calcite impurities in the sodium-based bentonite, which is corroborated by the peaks labeled as calcite (PDF#86-2334) in Figure S4. During the homogeneous mixing stage, the C–C bond and C–F bond cannot be detected in the C 1s and F 1s spectra owing to the enclosed polymer chains of PTFE; the C–C bond in the C 1s spectrum may originate from adventitious carbon and serves merely as a calibration reference. It is also supported by the Fourier Transform Infrared (FT-IR) spectrum provided in Figure S5a. Similarly, the C–O bond (286.54 eV) also originates from adventitious carbon. The characteristic peak at 1072.22 eV in

the Na 1s spectrum originates from the sodium-based bentonite. Upon the fibrillating stage, new peaks emerge in the C 1s spectrum, corresponding to the characteristic C–C peak and C–F peak of the $[-CF_2CF_2]_n$ structure in PTFE, situated at 284.8 eV and 292.40 eV , respectively. Meanwhile, this is affirmed in the FT-IR spectrum, where new peaks at 1151 and 1207 cm^{-1} can be observed, corresponding to the symmetric and asymmetric stretching of C–F and C–C stretching vibrations.^[42] The peak at 689.67 eV in the F 1s spectrum corresponds to the C–F bond in PTFE. In the kneading stage, due to the more extensive fibrillation of PTFE, the intensities of the C–C bond and C–F bond in the C 1s spectrum are enhanced. Furthermore, the formation of Na–F peaks becomes evident in both the F 1s and Na 1s spectra, with distinct peaks observed at 684.50 eV and 1071.20 eV , respectively. As shown in the Figure S5b, the Raman peaks of fluorine atoms^[43] reside within the range of 500 – 1000 cm^{-1} . After kneading, although Raman spectroscopy lacks the precision to differentiate between C–F and Na–F bond, these peaks exhibit significant intensification and multiplication, indicating the formation of additional fluorine-containing chemical bonds. These discoveries further substantiate the dependability of the theoretical calculations.

2.2. Electrochemical Characterization

To delve into the impact of Ben content on the electrochemical characteristics of MnO_2 solvent-free cathode (Ben-SFC), Ben-SFC//Zn full cells with same high areal loadings were employed for evaluation. Zn–In alloying powder solvent-free electrodes (Zn@In SFA) were served as anodes and as reported in our previous work and illustrated in the supporting information. Figure 4a displays the constant-current discharge/charge curves for each set of cells. To better mirror the behavior of actual batteries, it is advisable to normalize the calculation of areal capacity for each battery group by applying a uniform current density per unit area. When tested at a current density of 0.5 mA cm^{-2} , 0% Ben group exhibited the highest initial discharge capacity of 1.51 mAh cm^{-2} , while 7% Ben group, though lower at 1.30 mAh cm^{-2} , still maintained a considerable level. 1% Ben and 4% Ben groups fell in between, at 1.45 mAh cm^{-2} and 1.33 mAh cm^{-2} , respectively.

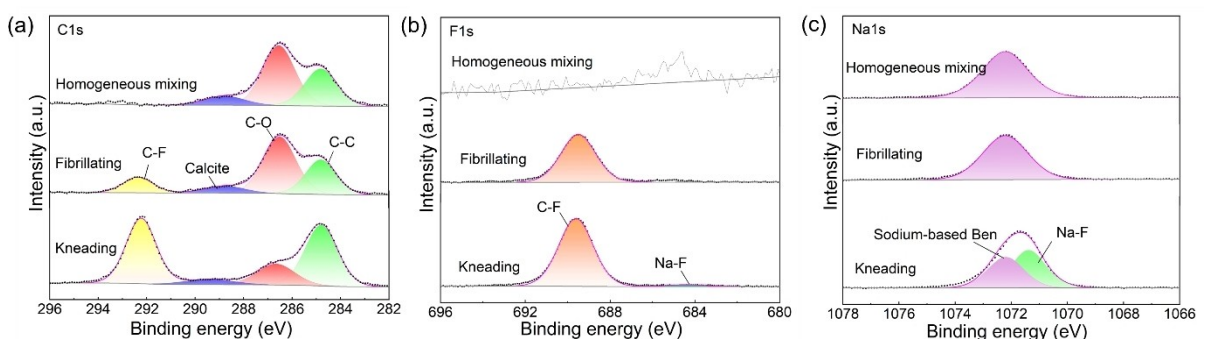


Figure 3. XPS spectra^[40–41] of a) C 1s, b) F 1s, c) Na 1s of sodium-based bentonite and PTFE mixture during the homogeneous mixing, fibrillating, and kneading stage.

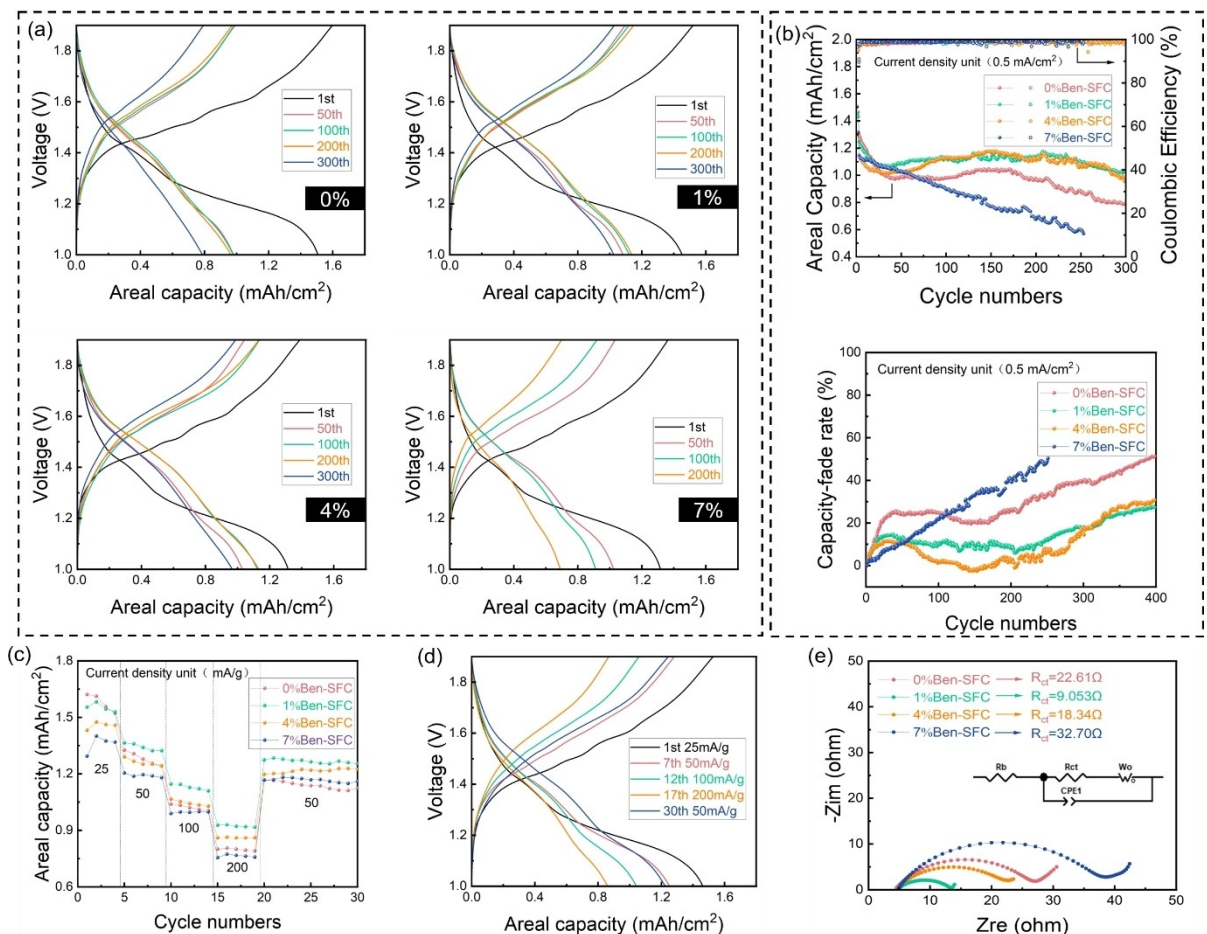


Figure 4. Performance of full cells assembled with Ben-SFC. a) Ben-SFC //Zn@In SFA with Ben content at 0%, 1%, 4%, and 7% corresponding galvanostatic discharge/charge curves of during 1st, 50th, 100th, 200th, and 300th cycles. b) Cycling curves of Ben-SFC//Zn@In SFA cells with different Ben content. c) Rate capability of Ben-SFC //Zn@In SFA cells from 25 mA g^{-1} to 200 mA g^{-1} . d) Discharge/charge curves of 4%Ben-SFC//Zn@In SFA cells at different rate capabilities. e) EIS spectra of each Ben-SFC//Zn@In SFA cells after cycle for the evaluation of R_{ct} .

Figure 4b illustrates the long-term cycling stability of the cells. All cells exhibited varying degrees of capacity fade, each displaying its own unique pattern. Within the initial 50 cycles, 0%Ben group entered a relatively stable phase of capacity fade the latest, with a significantly higher fade rate of 24.6% compared to 1%Ben (13.2%), 4%Ben (10.6%), and 7%Ben (11.0%). This indicates that the incorporation of Ben aids in reducing early capacity fade. From 50 to 200 cycles, except for 7%Ben group which continued to experience a decline in capacity, the other three groups demonstrated a notable trend of ‘climbing’ recovery, with the 4%Ben group showing the most significant recovery. Between 200 and 300 cycles, all cells show continuous capacity fade. By 300 cycles, 4%Ben group (with a fade rate of 14.8%) and 1%Ben group (with a fade rate of 18.1%) demonstrated relatively superior cycling stability, both significantly lower than 0%Ben group, which had a fade rate of 40%. Collectively, these findings suggest that moderate additions of Ben (e.g. 1%Ben and 4%Ben) can effectively slow dead Mn effect^[44] to some extent. However, the inherently poor conductivity of MnO_2 , coupled with the reduction in KS6 conductive graphite content due to excessive Ben, explains the

‘sliding’ capacity decline in 7%Ben group. Notably, the initial coulombic efficiency (CE) of all cells (Table S2) is around 90%, and it slowly increases over the subsequent few cycles, remaining relatively stable thereafter. This may be related to the pre-activation of the cell system, which enters a stable Zn ion migration shell layer is formed on the negative side.^[28] Additionally, all cells maintained a CE above 98% throughout long-term charge-discharge cycles, indicating the slow Mn death and Mn-based competitive capacity evolution,^[44] there were virtually no side reactions contributing to irreversible capacity loss.

Figures 4c-d and Figure S6 show the rate performance of the cells tested at different current densities. At a low current density of 25 mA g^{-1} , 0%Ben group again exhibited the highest initial discharge capacity, with 7%Ben group showing the lowest. However, at a high current density of 200 mA g^{-1} , the discharge capacity of 0%Ben group was only 49.6% of its initial value, lower than 54.7% retention of 7%Ben group. 1%Ben and 4%Ben groups excelled in rate performance, maintaining above 58% of their initial capacity. These findings indicate that addition of Ben also functions as a solid-state electrolyte,

facilitating charge transfer and enhancing rate capability of battery at high current densities. EIS measurements were used to characterize the charge transfer resistance (R_{ct}) of the cycled cells. As shown in Figure 4e, the Nyquist plots of all samples consist of a semicircle in the high-to-mid-frequency region and a slope in the low-frequency region. The semicircle in the high-to-mid-frequency region is attributed to the charge transfer of zinc ions at the electrode/electrolyte interface. The charge transfer resistance (R_{ct}) of the 0%Ben-SFC, which is unmodified with bentonite, is $22.61\ \Omega$. After incorporating bentonite, due to its porous structure and adsorption properties that facilitate electrolyte penetration and ion transport, the charge transfer resistance decreases, with the R_{ct} of 1%Ben-SFC being $9.065\ \Omega$. However, as the bentonite content increases, it may affect the fluidity of the electrolyte, and excessive additives may hinder ion transport at the electrode/electrolyte interface, resulting in an increase in charge transfer resistance to $18.34\ \Omega$ for 4%Ben-SFC and $32.7\ \Omega$ for 7%Ben-SFC. According to Table S1, the solution resistances of all samples are similar. This may be because bentonite primarily serves as an additive to improve

the performance of the MnO_2 cathode, and the addition amount within the range of 0% to 7% does not significantly alter the concentration of the electrolyte (or at least the degree of change is insufficient to significantly affect the solution resistance), thus the solution resistances of all samples are comparable, with a relatively small impact on the solution resistance.

To probe the structural evolution of cathode, Figures 5a-b present ex-situ XRD of Ben-SFC//Zn@In SFA cells, without and with bentonite, revealing a comparable redox behavior, suggesting that the addition of bentonite did not affect the redox reactions in the MnO_2 . Upon initial discharge, the characteristic peaks of $\epsilon\text{-MnO}_2$ are gradually weakened and new phase arises. Specifically, new peaks appear at 6.47° , 13.00° , 19.58° , and 32.93° , which can be attributed to reflections from the crystallographic planes of a layered Zn-buserite phase, analogous to previously reported.^[7] The exact structural motif of Zn-buserite is not determined yet, but will be further investigated in the future. In the followed charging process, the intensity of characteristic peaks for the layered phase was

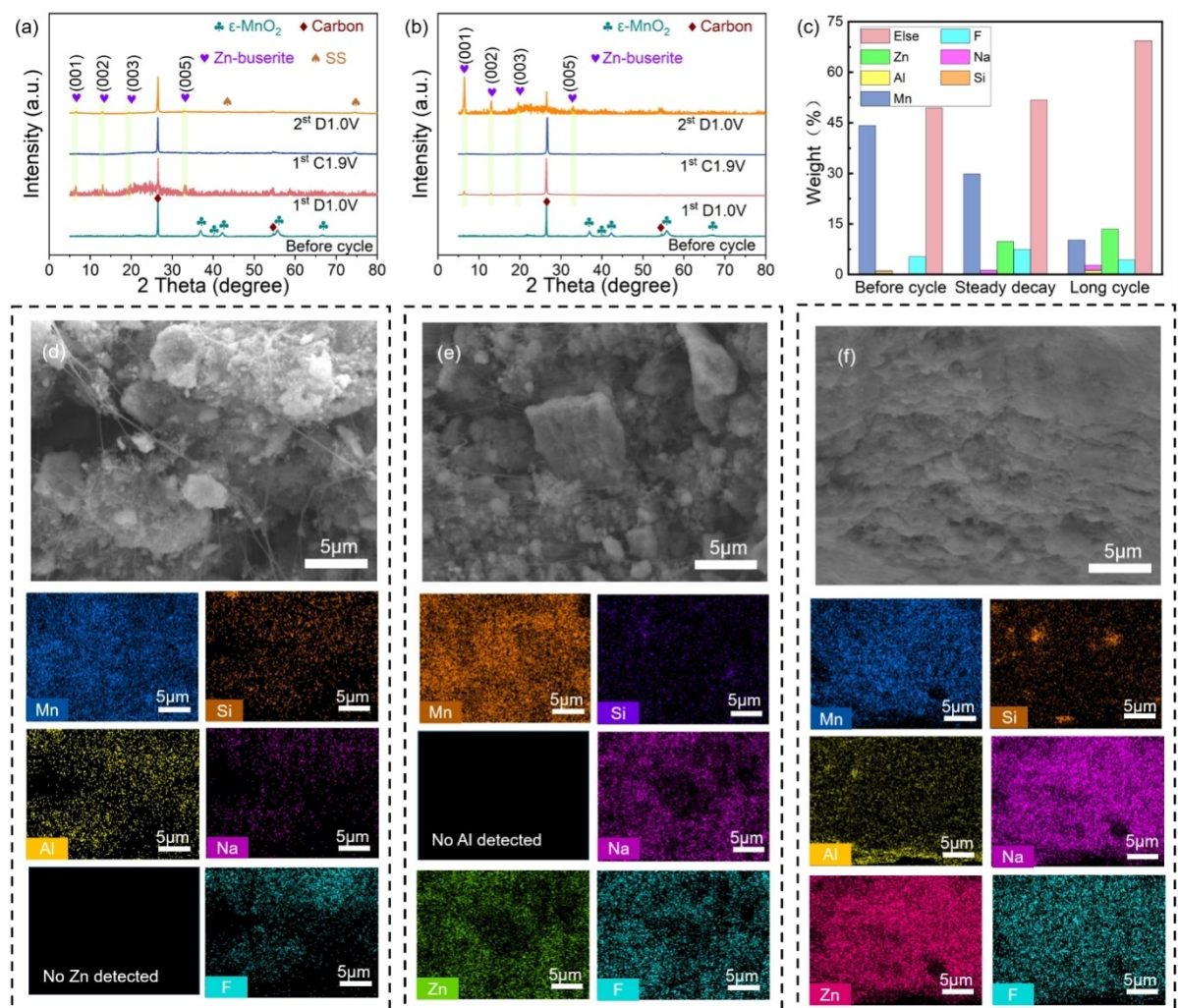


Figure 5. Electrochemical and structural evolution of cathode in Ben-SFC//Zn@In SFA cells. ex-situ XRD patterns of a) 0%Ben-SFC, b) 4%Ben-SFC. SEM images and corresponding EDS mapping of 4% Ben-SFC cross-sections d) before cycle, e) steady decay period, f) long cycle, along with c) a model depicting the element percentage accumulation.

gradually weakened upon extraction of Zn ions. This peak attenuation could be explained by the decrease of scattering atom concentration in unit cell and the weakening of Zn–O interaction due to Zn egress. Furthermore, a thorough analysis of 4%Ben-SFC was conducted at three stages: before cycle, during the stable decay period, and in the late stage of long-term cycle, using SEM and EDX. Combining elemental data from ‘before cycle’ in Figure 5c with the SEM image in Figure 5d, it is evident that basic constituent elements of Ben (such as Si, Al, Na, etc.) are highly consistent with the distribution of F element in PTFE, further validating the good combination of bentonite and PTFE observed in the simulation calculations. This combination enables the filamentous PTFE to better entangle MnO₂ powder and KS-6 conductive graphite, thereby creating an abundant specific surface area within the cathode, which facilitates the Mn ion and Zn ion transfer on the cathode side. During the stable decay period, according to relevant elemental data in Figure 5c, it was found that Mn element content decreased from an initial 44.2% to 29.8%, while Zn element content simultaneously reached 9.8%. This phenomenon can be attributed to the reaction of Zn²⁺ with the MnO₂ matrix form the Zn-buserite during discharge. In the subsequent charging process, Mn³⁺ undergoes disproportionation to form Mn²⁺, which dissolves in electrolyte. This cyclic process results in distortion of the MnO₂ internal structure, where MnO₂ appears as fragmented small clumps in Figure 5e. Notably, Na element can also be observed at this stage, possibly due to the weak intermolecular forces binding the bentonite layers, causing lamellar dissociation of bentonite as a result of cathode structure distortion. In the late stage of long-term cycle, Figure 5f shows severe collapse and even pulverization of the MnO₂ structure, along with significant damage to the bentonite structure. This leads to a significant decrease in Mn element content to 10.2%, while Zn element content increases to 13.5%. Simultaneously, Na and Al elements from bentonite are also prominently observed. This structural collapse may be caused by volume changes and stress accumulation resulting from prolonged charge-discharge cycles. The dissociation of bentonite further exacerbates the damage to the cathode structure, thereby affecting the battery cycling performance and energy density.

It is well-established that the pH value of cathode plays a crucial role in the electrochemical performance of aqueous Zn-ion batteries.^[28] When pH is close to neutrality, it effectively mitigates side reactions such as severe Mn²⁺ dissolution on cathode and hydrogen evolution, as well as Zn anode corrosion, thereby enhancing cycle stability and energy efficiency of battery. To further investigate, pouch cells were assembled and studied to delve into the regulatory effect of Ben content on the pH value of cathodes. As illustrated in Figure 6a, the pouch cell employed for testing comprised one Ben-SFC, one Zn@In SFA, and one PPS-SSS separator (same as our previous work), with the specific pH measurement method detailed in Figure S7.

As shown in Figure 6b, the results indicated that the aqueous solution of SFC cathode with 4% Ben content exhibited a pH of approximately 6.33, which is closer to

neutrality. In contrast, samples with 0% and 1% Ben content displayed weak acidity, while the sample with 7% Ben content performed even worse. We hypothesize that this phenomenon is attributed to the exchangeable cations (such as Na⁺, Ca²⁺, etc.) present in the interlayer spaces of Ben, which can influence the pH value of electrolyte through ion exchange mechanisms. As Ben content increases, the number of interlayer cations also rises, potentially leading to a more complex ion exchange process that drives pH value towards neutrality. Notably, the aqueous solution of 4% Ben-SFC, with a pH of around 6.33, provides favorable conditions for the insertion and extraction of Zn ions, effectively reducing Zn ion hydrolysis and the formation of byproducts in the electrolyte. Finally, we assembled an ampere-level pouch cell with 4% Ben-SFC for a constant discharge/charge performance test at a rate of 1.5 A, as depicted in Figure 6c. In the absence of air conditioning, the capacity of battery underwent notable fluctuations due to temperature disturbances during its initial 200 cycles. Following this, the battery sustained a capacity retention rate of 70% until 220th cycle. However, in the subsequent stages, the continuous decline in capacity may be attributed to the depletion of the electrolyte. When the concentration of the electrolyte is too high (3 M Zn(CF₃SO₃)₂ and 0.1 M MnSO₄), the sensitivity of the capacity to temperature becomes stronger and more volatile, which is also an urgent problem to be solved.

3. Conclusions

In summary, we successfully fabricated high-loading industrial-grade electrolytic MnO₂ cathodes (Ben-MnO₂-SFC) modified with sodium-based bentonite through a pilot-scale solvent-free dry process. The content of bentonite has a significant impact on the structure, mechanical properties, and electrochemical performance of the MnO₂ cathode. The sodium-based Ben enhances the structural stability of the electrode by forming Na–F bonds with polytetrafluoroethylene, demonstrated by both computational and XPS works. The Ben additives also can optimize H⁺ and Zn²⁺ transport through its ion-exchange properties to regulate pH. The high-loading Ben-SFC//Zn battery, with a loading exceeding 10 mg cm⁻², maintains a coulombic efficiency above 98% and capacity retention of 80%, even after approximately 400 cycles. Similarly, a 3Ah aqueous pouch cell demonstrates stable cycling over 400 times. By optimizing the combination of bentonite with other components, we anticipate further enhancing the cycle stability and energy efficiency of aqueous zinc-ion batteries.

We acknowledge funding from National Natural Science Foundation of China (Grants 51702131, 51774151, 22208130), Natural Science Foundation of Jiangsu Province, China (Grant SBK2017041705) and Norway-Jiangsu Industrial R&D Program (BZ2019021). This work was also supported by Institute of Green Materials and Metallurgy, Jiangsu University (Grant 5501670002). We acknowledge S. Yao, H. Zhu, R. Yan from Jiangsu Tongling Electric Co., Ltd. for the poilt line support (Grant HX230002). We acknowledge Dr. F. He and Dr. Qiu from

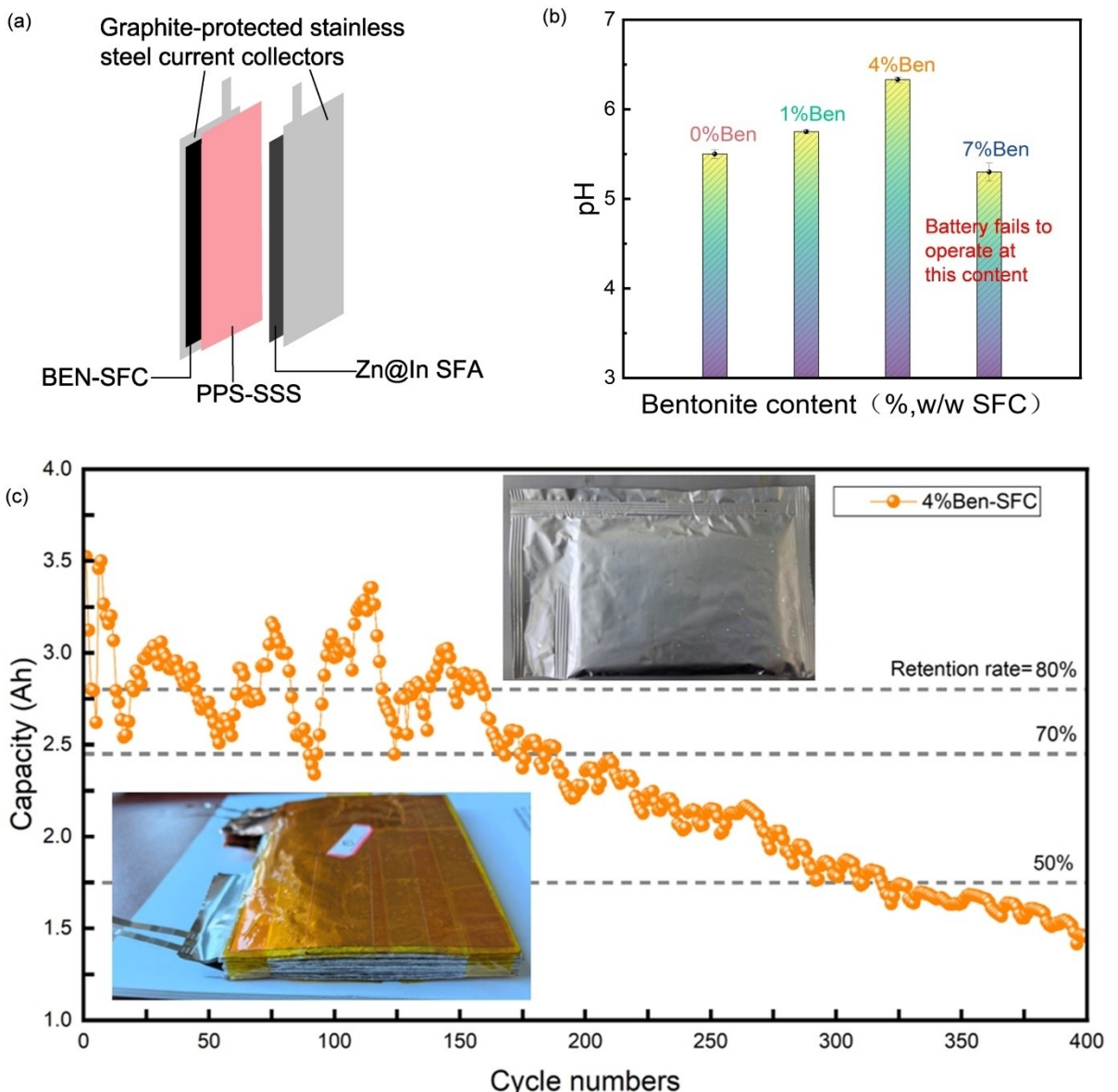


Figure 6. Performance and morphology of Ben-SFC pouch cells. a) Assembly diagram. b) The pH values of Ben-SFC. c)Cycling performance of Ben-SFC//Zn@In SFA pouch cell with 4%Ben content.

Zhuhai Energy New Materials Technology Co., Ltd. for the separator works.

Keywords: Zn-ion batteries · solvent free electrode · bentonite · MnO₂ cathode · high loadings

Conflict of Interests

The authors declare no conflict of interest.

Data Availability Statement

The data that support the findings of this study are available from the corresponding author upon reasonable request.

- [1] I. Hadjipaschalidis, A. Poulikkasis, V. Efthimiou, *Renewable Sustainable Energy Rev.* **2009**, *13*, 1513–1522.
- [2] S. Rana, R. Kumar, R. S. Bharj, *Chem. Eng. J.* **2023**, *463*, 142336.
- [3] Z. Xing, S. Wang, A. Yu, Z. Chen, *Nano Energy* **2018**, *50*, 229–244.
- [4] N. Dong, F. Zhang, H. Pan, *Chem. Sci.* **2022**, *13*, 8243–8252.
- [5] H. Jiang, W. Fan, *Eng. Agric.* **2023**, *43*.
- [6] W. Sun, F. Wang, S. Hou, C. Yang, X. Fan, Z. Ma, T. Gao, F. Han, R. Hu, M. Zhu, C. Wang, *J. Am. Chem. Soc.* **2017**, *139*, 9775–9778.
- [7] N. Zhang, F. Cheng, J. Liu, L. Wang, X. Long, X. Liu, F. Li, J. Chen, *Nat. Commun.* **2017**, *8*, 405.
- [8] P. He, Y. Quan, X. Xu, M. Yan, W. Yang, Q. An, L. He, L. Mai, *Small* **2017**, *13*, 1702551.
- [9] M. Yan, P. He, L. Mai, J. Yang, *ECS Meeting Abstracts* **2018**, MA2018-01, 56.
- [10] P. Canepa, G. Sai Gautam, D. C. Hannah, R. Malik, M. Liu, K. G. Gallagher, K. A. Persson, G. Ceder, *Chem. Rev.* **2017**, *117*, 4287–4341.

- [11] R. Trócoli, F. La Mantia, *ChemSusChem* **2015**, *8*, 481–485.
- [12] M. H. Alfaruqi, V. Mathew, J. Gim, S. Kim, J. Song, J. P. Baboo, S. H. Choi, J. Kim, *Chem. Mater.* **2015**, *27*, 3609–3620.
- [13] S. Islam, M. H. Alfaruqi, V. Mathew, J. Song, S. Kim, S. Kim, J. Jo, J. P. Baboo, D. T. Pham, D. Y. Putro, Y. Sun, J. Kim, *J. Mater. Chem. A* **2017**, *5*, 23299–23309.
- [14] Y. Jin, L. Zou, L. Liu, M. H. Engelhard, R. L. Patel, Z. Nie, K. S. Han, Y. Shao, C. Wang, J. Zhu, H. Pan, J. Liu, *Adv. Mater.* **2019**, *31*, 1900567.
- [15] Y. Li, S. Wang, J. R. Salvador, J. Wu, B. Liu, W. Yang, J. Yang, W. Zhang, J. Liu, J. Yang, *Chem. Mater.* **2019**, *31*, 2036–2047.
- [16] C. Xu, H. Du, B. Li, F. Kang, Y. Zeng, *Electrochem. Solid-State Lett.* **2009**, *12*, A61.
- [17] B. Lee, H. R. Seo, H. R. Lee, C. S. Yoon, J. H. Kim, K. Y. Chung, B. W. Cho, S. H. Oh, *ChemSusChem* **2016**, *9*, 2948–2956.
- [18] H. Pan, Y. Shao, P. Yan, Y. Cheng, K. S. Han, Z. Nie, C. Wang, J. Yang, X. Li, P. Bhattacharya, K. T. Mueller, J. Liu, *Nat. Energy* **2016**, *1*, 16039.
- [19] J. Yang, J. Cao, Y. Peng, W. Yang, S. Barg, Z. Liu, I. A. Kinloch, M. A. Bissett, R. A. W. Dryfe, *ChemSusChem* **2020**, *13*, 4103–4110.
- [20] X. Guo, J. Zhou, C. Bai, X. Li, G. Fang, S. Liang, *Mater. Today* **2020**, *16*, 100396.
- [21] X. Zeng, J. Liu, J. Mao, J. Hao, Z. Wang, S. Zhou, C. D. Ling, Z. Guo, *Adv. Energy Mater.* **2020**, *10*, 1904163.
- [22] A. Kausar, in *Hybrid Polymer Composite Materials* (Eds.: V. K. Thakur, M. K. Thakur, A. Pappu), Woodhead Publishing, 2017, pp. 115–132.
- [23] M. S. S. Kumar, N. M. S. Raju, P. S. Sampath, L. S. Jayakumari, *Reviews on advanced materials science* **2014**, *38*(1), 40–54.
- [24] T. D. Fornes, D. R. Paul, *Polymer* **2003**, *44*, 4993–5013.
- [25] X. Long, Z. Luo, W. Zhou, S. Zhu, Y. Song, H. Li, C. Geng, B. Shi, Z. Han, G. Zhou, W. Lv, J. Shao, *Energy Storage Mater.* **2022**, *52*, 120–129.
- [26] R. Shah, A. Kausar, B. Muhammad, S. Shah, *Polym.-Plast. Technol. Eng.* **2015**, *54*, 173–183.
- [27] C. Deng, X. Xie, J. Han, Y. Tang, J. Gao, C. Liu, X. Shi, J. Zhou, S. Liang, *Adv. Funct. Mater.* **2020**, *30*, 2000599.
- [28] X. Xie, H. Fu, Y. Fang, B. Lu, J. Zhou, S. Liang, *Adv. Energy Mater.* **2022**, *12*, 2102393.
- [29] W. Yao, M. Chouchane, W. Li, S. Bai, Z. Liu, L. Li, A. X. Chen, B. Sayahpour, R. Shimizu, G. Raghavendran, M. A. Schroeder, Y. Chen, D. H. S. Tan, B. Sreenarayanan, C. K. Waters, A. Sichler, B. Gould, D. J. Kountz, D. J. Lipomi, M. Zhang, Y. S. Meng, *Energy Environ. Sci.* **2023**, *16*, 1620–1630.
- [30] M. Ryu, Y. Hong, S. Lee, J. H. Park, *Nat. Commun.* **2023**, *14*, 1316.
- [31] H. Kim, J. H. Lim, T. Lee, J. An, H. Kim, H. Song, H. Lee, J. W. Choi, J. H. Kang, *ACS Energy Lett.* **2023**, *8*, 3460–3466.
- [32] F. Hippauf, B. Schumm, S. Doerfler, H. Althues, S. Fujiki, T. Shiratsuchi, T. Tsujimura, Y. Aihara, S. Kaskel, *Energy Storage Mater.* **2019**, *21*, 390–398.
- [33] J. Wu, X. Shen, H. Zhou, X. Li, H. Gao, J. Ge, T. Xu, H. Zhou, *Small* **2024**, *20*, 2308541.
- [34] H. Zhou, F. Ling, H. Zhou, J. Wu, X. Li, D. Hou, J. Ge, T. Xu, H. Gao, *J. Alloys Compd.* **2023**, *941*, 168886.
- [35] H. Zhou, M. Liu, H. Gao, D. Hou, C. Yu, C. Liu, D. Zhang, J. Wu, J. Yang, D. Chen, *J. Power Sources* **2020**, *473*, 228553.
- [36] H. Zhou, L. Wan, J. Han, J. Wu, Y. Deng, J. Gu, H. Wang, H. Gao, Z. Su, *Chem. Eng. J. Adv.* **2025**, *21*, 100694.
- [37] H. Zhou, C. Yu, H. Gao, J. Wu, D. Hou, M. Liu, M. Zhang, Z. Xu, J. Yang, D. Chen, *Small* **2021**, *17*, 2104365.
- [38] H. Zhou, M. Liu, Y. Li, C. Liu, H. Gao, Z. Cao, D. Zhang, X. Jin, Q. Chen, Y. Liu, J. Yang, *J. Electrochem. Soc.* **2018**, *165*, A3100.
- [39] C. Kim, Z. Akase, L. Zhang, A. H. Heuer, A. E. Newman, P. J. Hughes, *J. Solid State Chem.* **2006**, *179*, 753–774.
- [40] H. Chang, X. Liu, S. Zhao, Z. Liu, R. Lv, Q. Zhang, T. Yi, *Adv. Funct. Mater.* **2024**, *34*, 2313491.
- [41] T. Yi, L. Qiu, J. Mei, S. Qi, P. Cui, S. Luo, Y. Zhu, Y. Xie, Y. He, *Sci. Bull.* **2020**, *65*, 546–556.
- [42] R. Wang, G. Xu, Y. He, *e-Polym.* **2017**, *17*, 215–220.
- [43] D. H. Lemmon, *J. Mol. Struct.* **1978**, *49*, 71–82.
- [44] H. Yang, W. Zhou, D. Chen, J. Liu, Z. Yuan, M. Lu, L. Shen, V. Shulga, W. Han, D. Chao, *Energy Environ. Sci.* **2022**, *15*, 1106–1118.

Manuscript received: December 2, 2024

Revised manuscript received: February 26, 2025

Accepted manuscript online: February 27, 2025

Version of record online: March 7, 2025